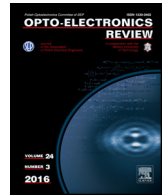




ELSEVIER

Contents lists available at ScienceDirect

Opto-Electronics Review

journal homepage: <http://www.journals.elsevier.com/opto-electronics-review>

Full length article

Power loss mechanisms in small area monolithic-interconnected photovoltaic modules

R. Kimovec^{a,*}, H. Helmers^b, A.W. Bett^b, M. Topič^a^a University of Ljubljana, Faculty of Electrical Engineering, Tržaška cesta 25, 1000 Ljubljana, Slovenia^b Fraunhofer Institute for Solar Energy Systems ISE, Heidenhofstr. 2, 79110 Freiburg, Germany

ARTICLE INFO

Article history:

Received 7 February 2018

Accepted 16 April 2018

Available online 1 May 2018

Keywords:

Monolithic interconnected photovoltaic module

Laser power converter

Optical and electrical losses

Current mismatch

Gaussian illumination

ABSTRACT

Power loss mechanisms in small area monolithic-interconnected photovoltaic modules (MIM) are described and evaluated. Optical and electrical losses are quantified and individual loss components are derived for loss mechanisms of small area radial (radius = 1 mm) pie-shaped six-segment GaAs MIM laser power converter. At low monochromatic homogeneous illumination ($G_{\text{low}} = 1.8 \text{ W/cm}^2$, $\lambda_0 = 809 \text{ nm}$) conversion efficiency of the cell, designed for a low irradiance, is reduced by 3.7%_{abs.} due to isolation trench optical losses and by 7.0%_{abs.} due to electrical losses (mainly perimeter recombination). Electrical losses in a device designed for a high irradiance, result in 18%_{abs.} decrease of output power under homogeneous monochromatic illumination ($G_{\text{high}} = 83.1 \text{ W/cm}^2$, $\lambda_0 = 809 \text{ nm}$), while 11.6%_{abs.} losses are attributed to optical reasons. Regardless the irradiance level, optical losses further increase if the device is illuminated with a Gaussian instead of an ideal flattop beam profile. In this case, beam spillage losses occur and losses due to isolation trenches and reflections from metallization are elevated. On top of that, additional current mismatch losses occur, if individual MIM's segments are not equally illuminated. For the studied device, a 29 μm off center misalignment of a Gaussian shaped beam (with 1% spillage) reduces the short circuit current I_{sc} by 10%_{abs.} due to the current mismatch between segments.

© 2018 Association of Polish Electrical Engineers (SEP). Published by Elsevier B.V. All rights reserved.

1. Introduction

The analysis of power loss mechanisms in photovoltaic (PV) devices provides us with an understanding of the energy flow from the incident light energy to the extracted electrical energy. Moreover, a quantitative assessment of individual power loss mechanisms enables a systematic understanding and paves the way towards improvements of the device.

In this work we present and structure power loss mechanisms in small area monolithic interconnected PV modules (MIM) [1]. Typical representatives of such devices are laser power converters (LPC) [2–5]; i.e., PV devices optimized for the conversion of monochromatic light in so called power-over-fiber (or power-by-light) systems [6]. Here, a monochromatic laser light is guided, typically through an optical fiber, to the remote location, where a LPC converts it into electricity to power electronic devices in harsh and extreme environments [7].

In this work, the assessment of general loss mechanisms (i.e., optical and electrical losses) is divided into a variety of sub-loss

mechanisms of small area MIMs. Furthermore, based on measurements, as well as simulations and theory, loss mechanisms in the real world six-segment MIM LPC are quantitatively assessed.

2. Overview of loss mechanisms in small area mim PV devices

Conversion efficiency (η) of photovoltaic devices is the most important figure of merit; quantitatively defining the ratio between the incident light power on the PV cell (P_{in}) and the extracted electrical power (P_{out}):

$$\eta [\%] = \frac{P_{\text{out}}}{P_{\text{in}}} \cdot 100\% \quad (1)$$

P_{in} is impaired by optical (L_{optical}) and electrical ($L_{\text{electrical}}$) losses, so we can formulate:

$$P_{\text{out}} = P_{\text{in}}(100\% - L_{\text{optical}} - L_{\text{electrical}}) \quad (2)$$

In the following both general loss mechanisms are analyzed and categorized for small area MIMs. A conceptual cross section of such devices is depicted in Fig. 1(a).

MIMs are commonly manufactured on a semi-insulating substrate, which serves as electrical isolation between adjacent PV

* Corresponding author.

E-mail address: rok.kimovec@fe.uni-lj.si (R. Kimovec).

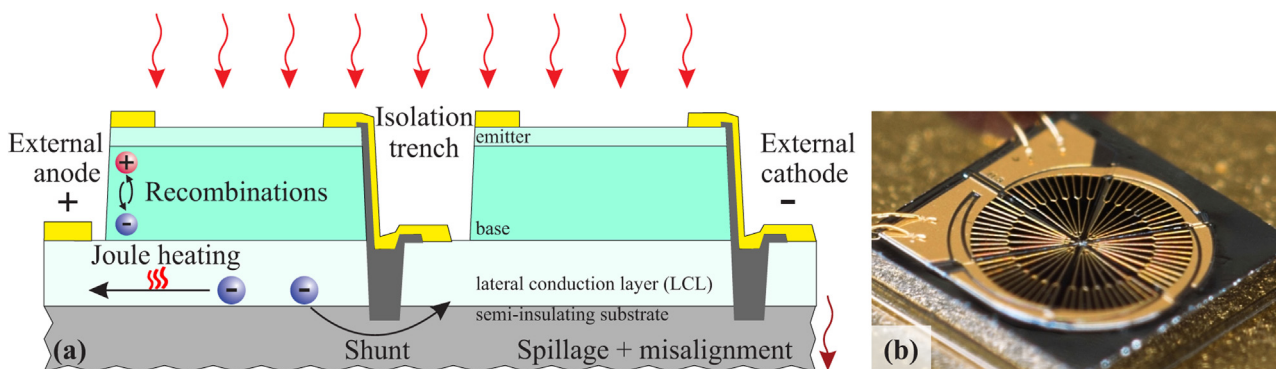


Fig. 1. (a) A conceptual cross section of a MIM PV device, showing series interconnection between photo active segments. Various loss mechanisms, as described in this paper, are shown in places of their origin. (b) A micrograph of the six-segment GaAs MIM LPC designed for high irradiance illumination. Series interconnections between adjacent segments are established outside the circular active area.

segments. The first layer grown on top of the substrate is a lateral conduction layer (LCL) that results in a low-ohmic structure for a lateral flow of photo generated current in the bottom of the individual MIM's segment. Low ohmic path for a lateral current flow in the top of the individual segment is achieved with a suitable design for the busbar and finger grid metallization. Isolation trenches etched all the way into the substrate electrically separate adjacent segments. The exposed open edges of the *pn*-junctions are coated with a dielectric material to prevent shunting of the individual segment from metal bridges used for the series interconnection of adjacent segments.

In MIM devices we can divide optical losses L_{optical} into the following components:

- Spillage (L_{spillage}),
- Shading from front metal finger grid (L_{shading}),
- Area loss due to isolation trenches ($L_{\text{isolation}}$) and
- Reflection from the active area ($L_{\text{reflection}}$)

whereas electrical losses $L_{\text{electrical}}$ consist of:

- Series resistance losses due to Joule heating (L_{joule}),
- Shunting losses (L_{shunt}) divided into shunting between segments ($L_{\text{shunt seg.}}$) and shunting of the *pn* junctions ($L_{\text{shunt pn.}}$),
- Minority carrier recombination ($L_{\text{recombination}}$) and
- Current mismatch due to misalignment ($L_{\text{misalignment}}$).

Some of the listed losses are common for all PV devices, while others are specific for MIMs. Furthermore, some of the loss mechanisms are common among all MIMs while others are device dependent. In the following paragraphs, we discuss and evaluate the loss mechanisms one-by-one. Beside general assessment of loss mechanisms in MIMs, we assess quantitatively the losses in real world small area six-segment GaAs MIM LPC pictured in Fig. 1(b) and thoroughly described in Refs. [3] and [18].

2.1. Optical losses (L_{optical})

Consideration of the optical loss contributions listed above leads to the following equation:

$$L_{\text{optical}} = L_{\text{spillage}} + (1 - L_{\text{spillage}}) (L_{\text{shading}} + L_{\text{isolation}} + L_{\text{reflection}}) \quad (3)$$

$(1 - L_{\text{spillage}})$ represents the fraction of the incident power that hits the designated area of the MIM ($A_{\text{designated}}$). Here, designated area is defined as the inner aperture area of the LPC (for the studied device this is circular area inside the busbars; compare Fig. 1(b)) and, therefore, follows the areal definition of small area PV devices [8].

2.1.1. Spillage losses (L_{spillage})

Spillage losses are frequently present in power-over-fiber systems since the power density profile at the output of an optical fiber is usually Gaussian (for single-mode fibers), or a superposition of Gaussian beams (for multi-mode fibers). Thus, due to the nature of a Gaussian distribution, a fraction of the light that exits the optical fiber does not impinge on the LPC's designated area, but hits the cell's surroundings:

$$L_{\text{spillage}} [\%] = \left(1 - \frac{P_{\text{designated}}}{P_{\text{total}}} \right) \cdot 100\% \quad (4)$$

where $P_{\text{designated}}$ is the power impinged on the designated area and P_{total} is the total power exiting the optical fiber.

Positioning of the fiber end in close proximity to the LPC can minimize spillage losses. Yet, that causes a strong non-uniformity of the irradiance distribution across the surface of the device, which leads to additional Joule heating losses compared to homogeneous illumination [9,10]. Therefore, in practical application a compromise must be found between spillage losses on the one hand and losses due to inhomogeneous illumination on the other. As a loose design rule, in practice, spillage losses in the order of 1%_{abs.} provide a good compromise. To reduce spillage losses, beam shaping techniques can be employed to transform a Gaussian beam to a flattop profile [11,12]. Such approaches can mitigate spillage losses and provide homogeneous illumination across the LPC, but are often too complex and not economic for most of the practical applications.

2.1.2. Shading losses (L_{shading})

Shading losses are common among all PV devices and MIMs are no exception. A front grid metallization, that provides low ohmic path for a lateral current flow in the top of PV devices, covers a part of the designated area ($A_{\text{designated}}$). Since the front metallization reflects or absorbs the impinging light, losses connected to the shading, for uniformly illuminated device, are directly proportional to the area covered by the front finger grid metallization ($A_{\text{grid metal}}$), as formulated in Eq. (5).

$$L_{\text{shading}} [\%] = \frac{A_{\text{grid metal}}}{A_{\text{designated}}} \cdot 100\% \quad (5)$$

For other illumination profiles (including Gaussian), a weighted L_{shading} can be derived from the convolution of the spatial irradiance profile $p_{\text{illum.}}(x,y)$ and the spatial distribution of a considered metallization area $A_{\text{metal}}(x,y)$, divided by the total power impinged on the designated area ($P_{\text{designated}}$), as seen in Eq. (6):

$$L_{\text{shading}} [\%] = \frac{\iint p_{\text{illum.}}(x,y) \cdot A_{\text{metal}}(x,y) dx dy}{P_{\text{designated}}} \cdot 100\% \quad (6)$$

For our calculations, we used a binary function for $A_{\text{metal}}(x,y)$, where 1 represents a complete reflection for areas covered by metal finger grid and 0 the active cell area. In practice, e.g., a non-rectangular shape of fingers can also result in apparent partial transparency of the metallization (and, thus, $0 < A_{\text{metal}}(x,y) < 1$) by redirecting some of the impinging light towards the active area [13].

The finger grid metallization is usually designed for a particular end application. For devices intended for high irradiances, dense finger grid metallization covers significant portion of the active area, whereas finger grid metallization can be omitted for devices intended for low irradiance; consequently, $L_{\text{shading}} = 0\%$ in such cases. For the studied sixsegment LPC [Fig. 1 (b)], that was designed for a high irradiances, the front metal finger grid covers approximately 7.9% of the designated area, therefore $L_{\text{shading}} \approx 7.9\%_{\text{abs}}$, if the device is illuminated homogeneously (flat-top illumination profile). Weighted shading losses for the studied device increase to $9.4\%_{\text{abs}}$, if we assume Gaussian illumination with 1% spillage. These two values indicate the importance of consideration of the actual spatial illumination profile and spatial metal distribution when calculating L_{shading} .

2.1.3. Isolation trench losses ($L_{\text{isolation}}$)

Losses due to isolation trenches are unique to MIMs and are present inherently by the design. As the isolation trench area is etched away to separate adjacent segments, they are straightforward areal losses. For a homogeneously illuminated device, $L_{\text{isolation}}$ can be calculated as:

$$L_{\text{isolation}} [\%] = \frac{A_{\text{trench}}}{A_{\text{designated}}} \cdot 100\%. \quad (7)$$

For the studied radial, pie-shaped MIM LPC designated area can be approximated as:

$$A_{\text{designated}} \approx \pi \cdot \text{radius}_{\text{LPC}}^2 \quad (8)$$

and for the same device we can approximate the total area of isolation trenches (A_{trench}) as:

$$A_{\text{trench}} \approx \text{radius}_{\text{LPC}} \cdot W_{\text{trench}} \cdot N_{\text{seg}} \quad (9)$$

where W_{trench} is the trench width, N_{seg} is the number of segments and $\text{radius}_{\text{LPC}}$ is the inner radius of the device (circular area inside the busbars). It follows:

$$L_{\text{isolation}} [\%] \approx \frac{W_{\text{trench}} \cdot N_{\text{seg}}}{\pi \cdot \text{radius}_{\text{LPC}}} \cdot 100\%. \quad (10)$$

For non-homogeneous illumination, again a convolution between the spatial illumination distribution $p_{\text{illum}}(x,y)$ and spa-

tial distribution of the isolation trenches $A_{\text{trench}}(x,y)$ can be used to obtain the weighted $L_{\text{isolation}}$:

$$L_{\text{isolation}} [\%] = \frac{\iint p_{\text{illum}}(x,y) \cdot A_{\text{trench}}(x,y) dx dy}{P_{\text{designated}}} \cdot 100\% \quad (11)$$

where $A_{\text{trench}}(x,y) = 1$ for the area etched away to form isolation trenches and $A_{\text{trench}}(x,y) = 0$ for all other areas.

Since the number of segments is typically defined by the desired output voltage, we can only reduce $L_{\text{isolation}}$ by either making trenches narrower or the whole device larger. A 1.04 mm radius and a nominal 20 μm trench width of studied six-segment MIM LPC results in $L_{\text{isolation}} \approx 3.7\%_{\text{abs}}$, when the device is illuminated homogeneously, while for the same device illuminated with Gaussian beam, assuming 1% spillage, $L_{\text{isolation}} = 7.3\%_{\text{abs}}$.

2.1.4. Reflection losses ($L_{\text{reflection}}$)

Reflection losses occur when an incident light is reflected from the surface of the active area, due to a difference in refractive indices between the air and used semiconductor. Texturing of surface and anti-reflection coatings are commonly used to mitigate reflection losses of PV devices. Contrary to the broadband illumination, where reflection losses cannot be completely eliminated, for monochromatic illumination an optimized antireflective front coating allows for a complete elimination of reflection losses [14].

2.2. Electrical losses ($L_{\text{electrical}}$)

As listed above, we consider electrical losses of four different origins:

$$L_{\text{electrical}} = L_{\text{Joule}} + L_{\text{shunt}} + L_{\text{recombination}} + L_{\text{alignment}} \quad (12)$$

The influence of Joule heating, shunting and recombination losses on the monochromatic ($\lambda_0 = 809 \text{ nm}$) conversion efficiency η at various irradiances for the studied six-segment MIM LPC is plotted in Fig. 2. The results are obtained with a verified distributed electrical model implemented in PVMOS [15], described in more details in Ref. 18. Yellow circles in Fig. 2 show a conversion efficiency of the device with all electrical loss mechanisms included in the model and serve as the reference case. For all other curves, the respective loss mechanism was excluded from the model. Consequently, a comparison of the individual curve with the reference case reveals the influence of the distinctive electrical loss mechanism on the device performance as a function of monochromatic irradiance.

Opposed to optical losses, which are independent on the irradiance G , the impinging power density has a significant influence

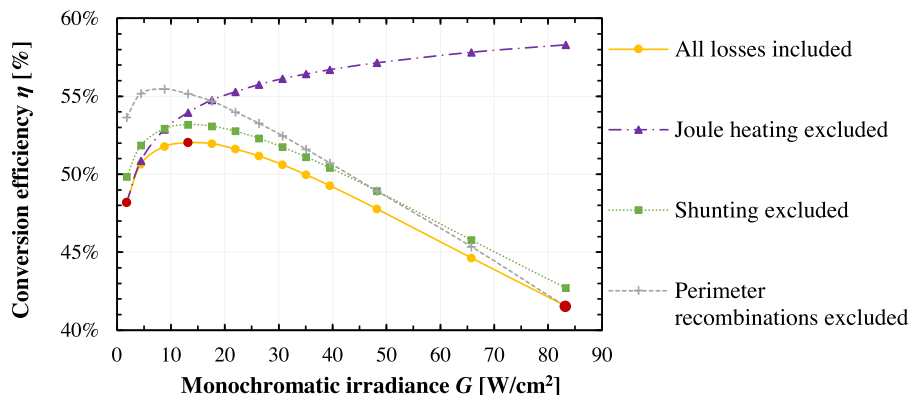


Fig. 2. Illustration of the influence of different electrical loss mechanisms on the conversion efficiency under homogeneous monochromatic ($\lambda_0 = 809 \text{ nm}$) irradiance for the studied sixsegment MIM LPC specimen. Red circles mark irradiances for further analysis, namely $G_{\text{low}} = 1.8 \text{ W/cm}^2$, $G_{\text{optimal}} = 13.2 \text{ W/cm}^2$, $G_{\text{high}} = 83.1 \text{ W/cm}^2$. Modified from Ref. [18].

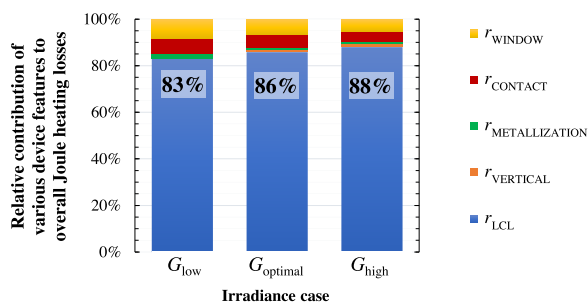


Fig. 3. Relative contributions of various features to overall Joule losses at three different irradiances: $G_{low} = 1.8 \text{ W/cm}^2$, $G_{optimal} = 13.2 \text{ W/cm}^2$, $G_{high} = 83.1 \text{ W/cm}^2$. Percentage figures in the columns present the relative contribution of the Joule heating in the LCL to the overall Joule heating losses.

on the magnitude of the different electrical losses. For low irradiance (G_{low}), minority carrier recombination processes (especially recombination at the perimeter of pn -junctions [16]) limit the performance. Majority carriers flow through the structure with a finite conductance results in a series resistance related Joule heating; the major loss mechanism at high irradiance (G_{high}). Shunting between the segments [17] reduces the efficiency for all irradiances equally by $1.2\%_{abs.}$, while the absolute value of the conversion efficiency at optimal irradiance ($G_{optimal} = 13.2 \text{ W/cm}^2$) is influenced by all loss mechanisms. In the following, the presented electrical loss mechanisms are described in more detail. A detailed analysis and comprehensive description of the simulation model and the individual loss mechanisms can be found in Ref. 18.

2.2.1. Joule heating – series resistance losses (L_{joule})

Joule heating losses in PV devices occur when the photo generated current flows towards the external terminals through different device features with a finite conductance (e.g., base, emitter, window, lateral conduction layer, metallization). The related loss effect is a transformation of electrical energy into heat. In the PV field Joule heating losses are commonly labeled as series resistance (R_s) losses.

For the studied device, relative contributions of various features to overall Joule losses are shown in Fig. 3 for three different irradiances. In this case, the significance of Joule heating regions, is in the following order:

- Sheet resistance of base plus the lateral conduction layer – r_{LCL}
- Sheet resistance of window plus emitter layer – r_{WINDOW}
- Specific contact resistance between front metallization and semiconductor – $r_{CONTACT}$
- Combined resistivity of the epitaxial layers for a vertical current flow through the active PV layers – $r_{VERTICAL}$
- Sheet resistance of metal grid fingers and busbars – $r_{METALLIZATION}$.

except for the low irradiance, where relative contribution of the Joule heating on the metallization is higher than relative contribution of the Joule heating due to vertical current flow through the device.

The distinct geometrical and crosssectional design of MIM devices results in a significant lateral current flow, especially in the lateral conduction layer (LCL) beneath the individual segments. For the investigated specimen this determines the major component of Joule heating losses. In absolute terms, for the studied device, combined Joule heating reduces efficiency by 0.3%, 1.9%, and 16.8% at low, optimal and high irradiance, respectively. For all studied cases more than 80% of combined Joule heating losses are caused by the lateral current flow in the LCL as seen in Fig. 3.

2.2.2. Shunt losses (L_{shunt})

Shunting in PV cells occurs due to an alternative path for the photo generated current flow in the device. In MIMs this current path can be established through the (typically semi-insulating) substrate between adjacent segments ($L_{shunt \text{ seg.}}$). The effect of inherently presented leakage current flow through the substrate (in μA range) is usually significant only at low irradiances and corresponding low operating currents (also in μA range). Effect of such low leakage current on the device performance diminishes at higher irradiances with corresponding operating currents in mA range or larger [17,19]. However, this is only true, if the substrate is not illuminated by the impinged light. We have recently shown [17], that in the studied device, significant shunting occurs between adjacent segments due to photo-induced conductivity in the semi-insulating GaAs substrate. This effect leads to an increased leakage current between adjacent segments and is responsible for a power loss of $1.2\%_{abs.}$ for all studied irradiances, which can be explained by the reciprocal relation between substrate resistivity and irradiance [17]. In comparison, in the studied device the effect of junction shunting ($L_{shunt \text{ pn.}}$) (commonly nominated with R_{sh} in the PV field) on the performance of the device, is negligible [18].

2.2.3. Recombination losses ($L_{recombination}$)

Minority carrier recombination losses occur when photo generated electron-hole pairs recombine before they are separated at the pn -junction. This process is the origin of the dark saturation current density J_{0n} , which also impairs the illuminated performance of the device. Since several recombination mechanisms are present in the PV cell, we normally classify them by the region of their origin and accordingly, each region is accompanied by its own J_{0n} . The absolute value of the distinct J_{0n} , in the combination with connected diode ideality factor n , influences the severity of the distinct recombination process with varying illumination. Due to the physical nature of different recombination processes, not all of them result in the same n and furthermore the values of n are usually limited to 1 or 2 [20].

With the experimentally validated model we found that significance of recombination region, for the investigated device, up to very high irradiance is in the following order [16,18,21]:

- Perimeter recombination (J_{02p} , $n = 2$)
- Neutral region recombination (J_{01} , $n = 1$)
- Depletion region recombination (J_{02b} , $n = 2$)

Where J_{02p} and J_{02b} are the perimeter and bulk components of J_{02} connected with the following equation [16]:

$$J_{02} = J_{02b} + \frac{P}{A} \cdot J_{02p}, \quad (13)$$

where P is the total perimeter of an individual MIM's segment and A is the total area of an individual MIM's segment pn -junction. Due to a multi-segment design and small areas, the perimeter to area ratio is high ($P/A = 57 \text{ cm}^{-1}$ for the sixsegment MIM LPC shown in Fig. 1). From Eq. (13) and absolute values of the dark saturation currents with $n = 2$ ($J_{02p} = 5 \cdot 10^{-12} \text{ A/cm}$, $J_{02b} = 2 \cdot 10^{-11} \text{ A/cm}^2$) we can calculate that perimeter recombination are the major contributing factor to recombination losses.

For the studied six-segment MIM LPC, the perimeter recombination reduces the peak conversion efficiency by $3.5\%_{abs.}$ at optimal monochromatic ($\lambda_0 = 809 \text{ nm}$) irradiance 13.2 W/cm^2 ; compared to the case, where J_{02p} was set to the value of J_{02b} in the model (compare grey squares and yellow circles in Fig. 2). At low irradiance ($G_{low} = 1.8 \text{ W/cm}^2$), the effect of the perimeter is even more pronounced and causes $5.5\%_{abs.}$ drop in efficiency. Only at very high irradiance ($G_{high} = 83.1 \text{ W/cm}^2$) perimeter recombination saturates

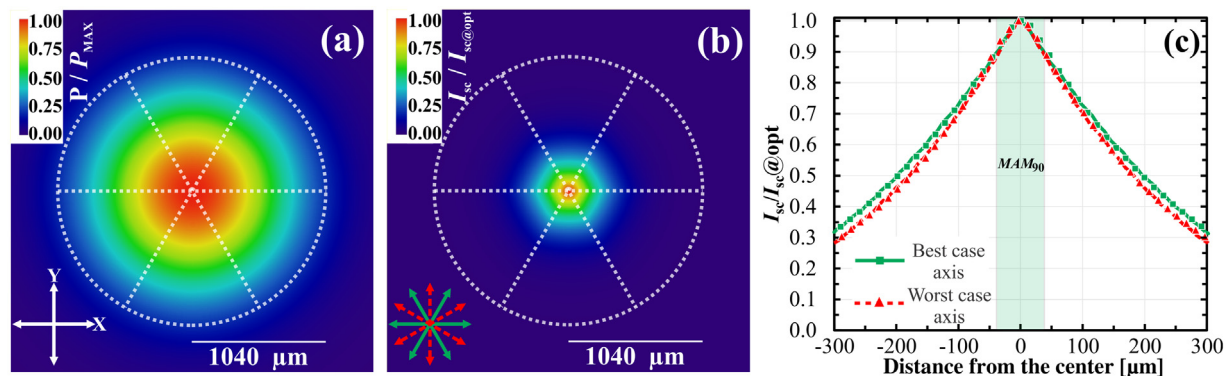


Fig. 4. (a) Normalized power density map of a Gaussian beam with 1% spillage, which is used for simulations of a current mismatch. A dashed white circle represents designated area of studied radial six-segment pie-shaped MIM ($radius_{LPC} = 1.04 \text{ mm}$), while arrows mark coordinate system. (b) Graphical representation of the drop of output current due to misalignment of the studied devices. Dotted white segmented circles represent the ideal centered position without current mismatch ($I_{sc@opt}$), whereas the compass in the bottom left highlights the worst (red dashed arrows) and the best (green arrows) case axes regarding misalignment. (c) Line scans through the center of the current misalignment spatial map for the worst and the best case axes. Marks presents measured value while lines present simulation. Shaded rectangle in the center represents a maximum acceptable misalignment tolerance (MAM_{90}) for the studied device and specified conditions.

and neutral region recombination becomes the dominant recombination mechanism [18].

2.2.4. Misalignment losses ($L_{misalignment}$)

Misalignment losses in power-over-fiber systems, produced by misaligning centre of the laser beam and centre of the LPC, can lead to a severe reduction of an overall system efficiency. Due to the series interconnection of individual PV segments in MIM LPCs, the photo current of the least illuminated segment determines the output current of the entire device and a current mismatch occurs. Electric power generated by the MIMs in the maximum power point (P_{mpp}) is the product of open circuit voltage (V_{oc}), fill factor (FF) and short circuit current (I_{sc}), and the influence of a current mismatch in the MIMs on the P_{mpp} is most severely expressed through the reduction of the I_{sc} (for a reasonable alignment precision). Consequently, the reduction of the power-over-fiber system efficiency is directly linked to the reduction of the short circuit current I_{sc} , due to the current mismatch. [22]

To study the effect of current mismatch and connected misalignment losses in MIM LPCs, arising in real world power-over-fiber systems, we performed simulations with an experimentally validated model. In this model the current of each segment is calculated as the convolution of spatial irradiance and spatial responsivity of the individual MIM's segment, for every position of the LPC in the Gaussian beam, as suggested in Ref. 22. From that analysis a normalized spatial map of the current mismatch $I_{sc \text{ mis.}}$ and related misalignment losses can be obtained as:

$$I_{sc \text{ mis.}}(x, y) [\%] = \frac{\min(I_{sc@seg1...n})_{\lambda_{v}(x,y)}}{I_{sc@opt}} \quad (14)$$

where the numerator presents the I_{sc} of the least illuminated segment for the respective x, y misalignment position of the MIM LPC in the beam and the denominator ($I_{sc@opt}$) presents I_{sc} in the perfectly aligned position, i.e. current matched conditions (assuming the same light source).

This model was experimentally validated according to the following procedure: A six-segment MIM LPC was moved in (x, y) directions in $15 \mu\text{m}$ steps under fixed illumination with a Gaussian shaped laser beam. At each step the short circuit current was recorded with a Keithley 236 precision source/measurement unit (SMU). The power of the single mode fiber coupled diode laser (Thorlabs LPS-638-FC $\lambda_0 = 638 \text{ nm}$, $P_{max} = 6.7 \text{ mW}$) was actively kept constant with Thorlabs T-Cube Laser Diode Driver set to a constant power mode. A single lens was used to narrow the laser beam so that 1% of the beam spillage occurred. With this procedure a

spatial map of measured $I_{sc \text{ mis.}}(x, y)$ was obtained. The measured spatial map was normalized to the maximum value of the $I_{sc@opt}$ and two distinct line scans through the center of the spatial map ($I_{sc@opt}$) were extracted. Likewise, the line scans in the same directions were also extracted from the simulated $I_{sc \text{ mis.}}(x, y)$ spatial map. The deviation between normalized simulated and measured $I_{sc \text{ mis.}}$ line scans for the range $I_{sc \text{ mis.}}/I_{sc@opt} > 0.3$ was less than 0.2% [compare Fig. 4(c)], thus the model was experimentally validated.

The graphical normalized spatial representation of the simulated current mismatch $I_{sc \text{ mis.}}(x, y)$ for the studied six-segment radial ($radius_{LPC} = 1.04 \text{ mm}$) pie-shaped MIM is shown in Fig. 4(b), assuming Gaussian beam illumination with 1% spillage. Such spatial map presents fraction of I_{sc} of the limiting MIM's segment in every position of the MIM in the laser beam, compared to the optimally illuminated device (center position; $I_{sc@opt}$) and, therefore, directly corresponds to the misalignment losses $L_{misalignment}$.

From Fig. 4 we can see that the short circuit current reaches its maximum, when the device is positioned in the centre of the beam (as illustrated with dotted white segmented circle). Misalignment away from the centre in any direction quickly leads to a drop of the output current and a corresponding drop of the output power. In agreement with the predictions in Ref. 22, the drop of I_{sc} depends on the direction of the misalignment. We observe the best case misalignment in the axis of isolation trenches and the worst case in the direction in-between two adjacent trenches [noted with full green arrows for the best axis and with red dashed arrows for the worst axis in the bottom left corner in Fig. 4(b)]. For the worst case axis, the alignment positions of the MIM in the laser beam are the strictest, since the displacement of the device from the center leads to the highest current loss, while for the best case axis the equal displaced yields the lowest loss. Consequently, for this case the restriction for the MIM's precise alignment in the beam is eased.

To quantitatively define the maximum acceptable misalignment and compare different designs of MIMs, a suitable figure of merit is needed. In small area PV devices this is defined by the MAM_{90} – maximum acceptable misalignment from the center where 90% of the I_{sc} compared to $I_{sc@opt}$ is achieved [22]. Fig. 5 shows the simulated MAM_{90} for the studied pie-shaped six-segment MIM (illuminated with a Gaussian beam) as a function of the beam spillage for displacement along the best and the worst case axes. We can observe that increased spillage (larger or broader beam spot) loosens the alignment tolerance on the account of increased optical losses. Furthermore, increased spillage results in slight increase in the relative difference between MAM_{90} for the worst and the best case scenario. For the sixsegment MIM LPC with radius 1.04 mm

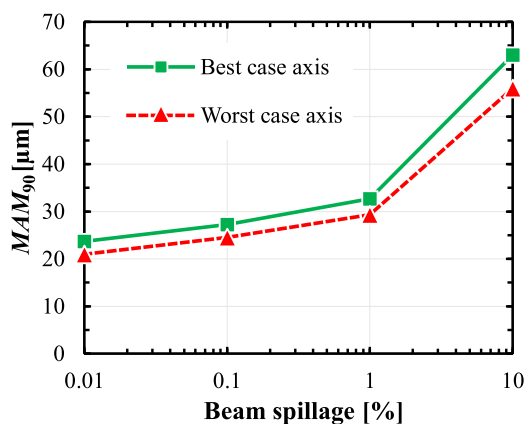


Fig. 5. Plot of the modeled maximum acceptable misalignment along the worst and the best case axes that results in a 10% current drop (MAM_{90} , compare Ref. [22]) for a radial six-segment pie-shaped MIM illuminated with a Gaussian beam as a function of assumed beam spillage.

and a beam spillage of 10%, a misalignment of only 56 μm already results in a current drop of 10%, assuming the worst case scenario. For a beam spillage of 1%, this value even drops further to 29 μm .

We conclude that current mismatch due to misalignment of the MIM LPCs is a severe problem and precise positioning in packaging must be achieved to realize good performance of power-over-fiber systems.

3. Conclusions

In this work we assessed the influence of various loss mechanisms on the performance of small area monolithically interconnected PV modules (MIM). Optical and electrical losses were divided into individual sub-components. Origins of considered loss components were discussed and a general assessment of their influence on the performance of small area MIMs was provided. Additionally, quantitative assessment of the individual loss components was presented for the investigated small area six-segment MIM laser power converter (LPC) specimen. We showed how electrical losses depend on the irradiance, while optical losses depend on the spatial profile of the irradiance and the spatial distribution of geometrical features of the device (e.g., distribution of the finger grid metallization).

Performance of the investigated device, under low homogeneous monochromatic ($\lambda_0 = 809 \text{ nm}$) illumination ($G_{\text{low}} = 1.8 \text{ W/cm}^2$), is predominantly impaired by perimeter recombination which causes 5.5%_{abs.} drop in efficiency. At high irradiance ($G_{\text{high}} = 83.1 \text{ W/cm}^2$) Joule heating (especially in the lateral conduction layer) limits the performance of the studied six-segment MIM LPC which results in a 16.8%_{abs.} drop of efficiency. For the investigated specimen, photo-induced leakage currents through the semi-insulating GaAs substrate reduce efficiency by 1.2%_{abs.}, regardless of the irradiance.

For optical losses we considered homogeneous (flat-top) and Gaussian monochromatic ($\lambda_0 = 809 \text{ nm}$) illumination of the six-segment laser power converter. Under monochromatic illumination, an optimized anti-reflective front surface allows for almost complete elimination of reflection losses for all the irradiances. We found that optical losses are the smallest for homogeneously illuminated low power devices, where we can omit finger grid metallization and in such case only isolation trench losses are unavoidable. For the studied device, under uniform illumination, isolation trench losses contribute roughly 3.7%_{abs.} to the overall lost power. For the same device and Gaussian illumination profile, $L_{\text{isolation}}$ increase to 7.3%_{abs.} and an additional 1%_{abs.} beam spillage

loss must be taken into account. For high power applications, additional optical losses occur due to front metal finger grid coverage. In the studied homogeneously illuminated device, with a finger grid metallization designed for a high irradiance illumination, 7.9%_{abs.} power is lost due to metallization shading. Similarly to the isolation trench losses, shading losses of such device increase under Gaussian illumination; for the same device this value increase from 7.9%_{abs.} to 9.4%_{abs.} In the worst case scenario presented in this work, optical losses add up to 17.7%_{abs.}

Finally, strict alignment tolerances must be kept to ensure good power-over-fiber system efficiency. Only 29 μm off-center position of the optical fiber (with Gaussian beam profile and spillage of 1%) to the LPC ($\text{radius}_{\text{LPC}} = 1.04 \text{ mm}$) results in a large current mismatch among segments and produces 10% reduction of the short circuit current for the studied device.

Acknowledgement

The authors acknowledge the financial support from the Slovenian Research Agency (program P2-0197 and PhD funding for R.K.).

References

- [1] A. Datas, P.G. Linares, Monolithic interconnected modules (MIM) for high irradiance photovoltaic energy conversion: a comprehensive review, *Renew. Sustain. Energy Rev.* 73 (2017) 477–495, <http://dx.doi.org/10.1016/j.rser.2017.01.071>.
- [2] V. Andreev, V. Khvostikov, V. Kalinovsky, V. Lantratov, V. Grilikhes, V. Rummyantsev, et al., High current density GaAs and GaSb photovoltaic cells for laser power beaming, *Proc. of 3rd World Conference on Photovoltaic Energy Conversion vol. 1* (2003) 761–764.
- [3] J. Schubert, E. Oliva, F. Dimroth, W. Guter, R. Loeckenhoff, A.W. Bett, High-voltage GaAs photovoltaic laser power converters, *IEEE Trans. Electron Devices* 56 (2009) 170–175, <http://dx.doi.org/10.1109/TED.2008.2010603>.
- [4] R. Kimovec, H. Helmers, A.W. Bett, M. Topič, Temperature and injection current dependent electroluminescence for evaluation of single-junction single-segment GaAs laser power converter, *Informacije MIDEM - J. Microelectron. Electron. Comp. Mater.* 46 (2016) 142–148.
- [5] M. York, S. Fafard, High efficiency phototransducers based on a novel vertical epitaxial heterostructure architecture (VEHSA) with thin p/n junctions, *J. Phys. D Appl. Phys.* 50 (173003) (2017), <http://dx.doi.org/10.1088/1361-6463/aa60a6>.
- [6] G. Bottger, M. Dreschmann, C. Klamouris, M. Hubner, M. Roger, A.W. Bett, et al., An optically powered video camera link, *IEEE Photon. Technol. Lett.* 20 (2008) 39–41, <http://dx.doi.org/10.1109/LPT.2007.912695>.
- [7] K. Worms, C. Klamouris, F. Wegh, L. Meder, D. Volkmer, S.P. Philipps, et al., Reliable and lightning-safe monitoring of wind turbine rotor blades using optically powered sensors: Rotor blade condition monitoring using optically powered sensors, *Wind Energy* 20 (2017) 345–360, <http://dx.doi.org/10.1002/we.2009>.
- [8] C. Algora, I. Rey-Stolle, G.R. Siefert, C. Osterwald, Area measurement, in: *Handbook on Concentrator Photovoltaic Technology*, John Wiley & Sons, 2016, p. 603.
- [9] V. Andreev, V. Grilikhes, V. Rummyantsev, N. Timoshina, M. Shvarts, Effect of nonuniform light intensity distribution on temperature coefficients of concentrator solar cells Osaka, Japan, *Proc. of 3rd World Conference on Photovoltaic Energy Conversion, 2003 vol. 1* (2003) 881–884.
- [10] I. Garcia, C. Algora, I. Rey-Stolle, B. Galiana, Study of non-uniform light profiles on high concentration III-V solar cells using quasi-3D distributed models San Diego, CA, USA, *Proc. of the 33rd IEEE Photovoltaic Specialists Conference (PVSC)* (2008) 1–6, <http://dx.doi.org/10.1109/PVSC.2008.4922908>.
- [11] K. Fuse, Beam shaping for advanced laser materials processing, *Laser Technik J.* 12 (2015) 19–22, <http://dx.doi.org/10.1002/latj.201500011>.
- [12] B. Hracek, H. Bäuerle, New ways to generate flat-top profiles, *Optik Photonik* 10 (2015) 16–18, <http://dx.doi.org/10.1002/opph.201500037>.
- [13] A.W. Blakers, Shading losses of solar-cell metal grids, *J. Appl. Phys.* 71 (1992) 5237–5241, <http://dx.doi.org/10.1063/1.350580>.
- [14] R. Kimovec, M. Topič, Comparison of measured performance and theoretical limits of GaAs laser power converters under monochromatic light, *Facta Universitatis - Ser.: Electronics Energetics* 30 (2017) 93–106, <http://dx.doi.org/10.2298/FUEE1701093K>.
- [15] B.E. Pieters, A free and open source finite-difference simulation tool for solar modules Denver, CO, USA: IEEE, *Proceedings of the 40th IEEE Photovoltaic Specialist Conference (PVSC)* (2014) 1370–1375, <http://dx.doi.org/10.1109/PVSC.2014.6925173>.
- [16] T.B. Stellwag, P.E. Dodd, M.S. Carpenter, M.S. Lundstrom, R.F. Pierret, M.R. Melloch, et al., Effects of perimeter recombination on GaAs-based solar cells Kissimmee, FL, USA, *Proc. of the 21st IEEE Photovoltaic Specialists Conference (PVSC) vol. 1* (1990) 442–447, <http://dx.doi.org/10.1109/PVSC.1990.111663>.

- [17] R. Kimovec, H. Helmers, A.W. Bett, M. Topič, On the influence of the photo-induced leakage current in monolithically interconnected modules, *IEEE J. Photovolt.* (2018) 1–6, <http://dx.doi.org/10.1109/JPHOTOV.2017.2783844>.
- [18] R. Kimovec, H. Helmers, A.W. Bett, M. Topič, Comprehensive Electrical Loss Analysis of Monolithic Interconnected Multi-Segment Laser Power Converters. Submitted for Publication.
- [19] Y. Wang, N. Chen, X. Zhang, Y. Bai, Y. Wang, T. Huang, et al., Analysis of leakage current in GaAs micro-solar cell arrays, *Sci. China Technol. Sci.* 53 (2010) 1240–1246, <http://dx.doi.org/10.1007/s11431-010-0003-x>.
- [20] K.R. McIntosh, South Wales, in: *Lumps, Humps and Bumps: Three Detrimental Effects in the Current-voltage Curve of Silicon Solar Cells*, University of New, 2001, Doctoral dissertation <http://handle.unsw.edu.au/1959.4/54714>.
- [21] P. Espinet-González, I. Rey-Stolle, M. Ochoa, C. Algora, I. García, E. Barrigón, Analysis of perimeter recombination in the subcells of GaInP/GaAs/Ge triple-junction solar cells: analysis of perimeter recombination, *Prog. Photovolt. Res. Appl.* 23 (2015) 874–882, <http://dx.doi.org/10.1002/pip.2501>.
- [22] L. Wagner, A.W. Bett, H. Helmers, On the alignment tolerance of photovoltaic laser power converters, *Optik* 131 (2017) 287–291, <http://dx.doi.org/10.1016/j.ijleo.2016.11.072>.